Versatile Acoustic Shadow Detection from Scanline Statistics of Brightness-Mode and Radiofrequency Ultrasound Images

Ricky Hu, Rohit Singla, Farah Deeba, and Robert N. Rohling

An acoustic shadow is an ultrasound imaging artefact which results in a continuous dark region beyond a boundary between two materials of significant impedance difference. Identifying acoustic shadows is clinical important as a shadow can indicate features such as calcifications, poor transducer contact, or lesions. Shadows also obscure anatomy beyond the shadowing boundary and thus, the detection of acoustic shadows is important in interpreting ultrasound images. In addition, the emergence of increasingly accessible ultrasound devices creates a need for feature recognition that can be applied for different equipment or anatomy with minimum expert configuration required. We propose a statistical technique for shadow detection that characterizes patches of radiofrequency speckle based on the scattering of acoustic waves in different materials, which is a unique feature that can be extracted from ultrasound imaging. We also propose a statistical detection method, a modified one-parameter algorithm that combines previous intensity and geometric methods, on brightness-mode images if radiofrequency data is not available. The detection methods achieved a Dice coefficient of 0.93±0.07 and 0.91±0.05 respectively when compared to the gold standard of manual detection. The methods presented require only the transducer pulse width as an input parameter and has been demonstrated to detect shadows on different transducers, transducer settings, and anatomy. Acoustic shadow detection has potential to be a valuable clinical asset in efficiently identifying features such as kidney stones or assist in artificial intelligence methods that require labelled ultrasound images.

I. INTRODUCTION

ULTRASOUD is a popular imaging modality as it provides real-time imaging, is relatively low cost compared to computed tomography of magnetic resonance imaging, and does not produce ionizing radiation. Recently, ultrasound devices have become increasingly affordable and portable [1], encouraging novice users or point-of-care ultrasound to be adopted more frequently [2-6]. However, ultrasound is susceptible to unique imaging artefacts that may cause the interpretation of images may be difficult, particularly for novice users. One such artefact is an acoustic shadow. An acoustic shadow occurs when an ultrasound wave from a transducer surface propagates towards a boundary of two materials with significantly different wave impedance properties [7]. The ultrasound wave is then mostly reflected, resulting in a loss of signal beyond the boundary. On an ultrasound brightness-mode (B-Mode) image, this appears as a sudden dark region at all

depths beyond the boundary. Acoustic shadows are significant as they are an asset and detriment in ultrasound imaging. Acoustic shadows are known to occur at air-tissue [8], tissue-bone [9, 10], and tissue-lesion [11] interface. By observing an acoustic shadow, we can deduce the presence of an air gap due to bad transducer contact, calcifications in tissue, or lesions depending on the context of the imaging location. Acoustic shadows have been leveraged to identify gall stones [10] or track the size of kidney stones [12]. However, acoustic shadows prevent the visualization of anatomical detail of regions axially deeper than the boundary, increasing the difficulty of interpreting images. Thus, the identification of shadows is important for the analysis of ultrasound images.

The interpretation of acoustic shadows is commonly performed by manual inspection from an expert, such as a radiologist. However, there are several motivations for the automatic detection of acoustic shadows. First, users with less sonography experience could interpret ultrasound imagery easier with acoustic shadows automatically identified. Secondly, acoustic shadows limit the capability of automated image processing. Modern analysis techniques involving images with shadows such as 3D reconstruction [12], fiducial registration [13], and training of supervised learning algorithms [14] require features to be identified or flagged as a shadow, which is time consuming if done manually.
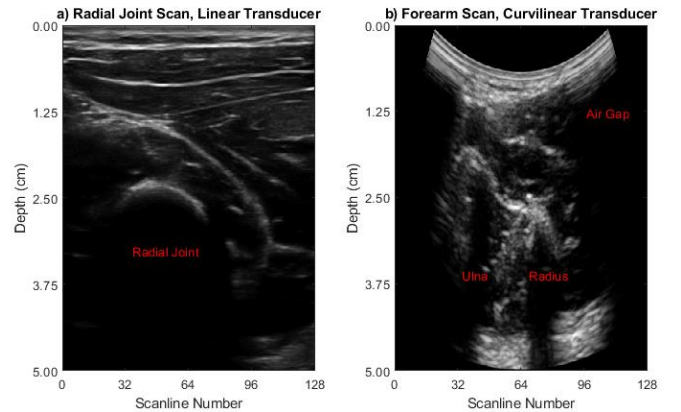

Fig. 1. Examples of acoustic shadowing, including a) shadowing due to a tissue-bone boundary at the radial joint near the elbow, b) shadowing due to a

tissue-bone boundary at the radius and ulna and shadowing due to an air gap created by poor transducer contact at the two lateral ends.

There are several existing techniques to automatically detect shadows which all report high similarity when compared to the gold standard of manual shadow detection [15-21]. However, existing techniques require several manually tuned parameters for different ultrasound machines, transducer geometries, and anatomy. As there exists a strong motivation to increase the usability of ultrasound for novice users, a shadow detection method with minimal configuration that requires knowledge of ultrasound machine properties is desired.

We present shadow detection methods based on analysis of scanline statistics from either radiofrequency (RF) and B-Mode data that requires only the transducer pulse width as an input parameter. The detection method was designed to detect shadows from multiple anatomical locations, depths, and transducers.

II. EXISTING WORK

Several methods have been developed to detect acoustic shadows, though the motivation was possibly limited in the past as manual shadow detection may have been sufficient before recent needs. Motivations for shadow detection are becoming increasingly stronger as point-of-care ultrasound and large-scale image processing algorithms are emerging.

Geometric methods have been used to compare an expected intensity profile given the physical characteristics of a specific ultrasound probe. Penney et al. (2004) detected shadows for by comparing freehand 3D ultrasound images of a liver for image registration from preoperative to intraoperative images [21]. The registration was robust, which was defined as below a 4% failure rate, for 4 out of 5 data sets. While this method was capable of detecting shadows for 3D reconstruction, the method required custom modelling of the expected image mask with properties of a specific ultrasound probe.

Random walks have also been previously implemented to model the path of an ultrasound signal. Karamalis et al. (2012) develop a random walk method to estimate a confidence map of an ultrasound image [15]. Certain regions can be flagged as a shadow if the detected pixel is below a confidence threshold. The shadow regions detected were compared with regions outlined manually by an ultrasound expert with Dice coefficient of 0.87 ± 0.05, indicating high similarity between automated and manual detection. However, the technique relies on knowing several ultrasound transducer properties such to assign weights in the random walk.

Pixel intensity methods have also been used to avoid parameterization based on the transducer. Hellier et al. (2010) detected acoustic shadows in ultrasound brain images by analyzing the statistical distribution of pixel intensities [16]. A "rupture criterion" was used by computing the entropy of pixels along the scanline and flagging pixels with high intensity as potential shadow artifacts. The flagged pixels were compared

to a parameterized noise model to identify if the pixel is associated with noise or a shadow. The detected shadow regions were compared with regions outlined with four experts, and a Dice coefficient above 0.817 was obtained comparing the detected region with four raters. However, thresholding, window sizes, filtering, and masking the image required specific parameter tuning of the algorithm for different anatomy.

Recently, deep learning methods have gained significant interest in ultrasound analysis, including images containing acoustic shadows. Milletari et al. (2017) [22] utilized a convolutional neural network modified with a Hough Forest to identify regions of cranial ultrasound images. Artificial intelligence methods are gaining further popularity as they are capable of abstracting the complexity of medical images to identify features based on recognition from similar images. However, this is difficult when insufficient data is available to train an artificial intelligence algorithm. For standardized images such as a MRI scan of the brain or X-Ray of the chest, the images are relatively consistent in orientation. However, ultrasound imaging is highly variable due to unique ultrasound artefacts, operator technique, and equipment. Thus, it is difficult to construct a training set of consistent images and further difficult to have sufficient imaging scenarios trained, such as different speckle patterns from thicknesses of muscle for different patients, to provide the generality required to recognize features. Deep learning methods are valuable for specific ultrasound applications, such as the detection of spinal levels demonstrated by Hetherington et al. (2017) [23]. However, acoustic shadows occur in many different imaging scenarios. It is then difficult to train an artificial intelligence method that can provide generalized shadow detection usable by clinicians for different ultrasound applications.

The method presented in this paper aims to be applicable for different anatomy and equipment, to minimize the amount of parameterization requiring manual tuning, and provide high accuracy for shadow detection.

III. METHODS

We present a shadow detection method utilize RF data and we also present a similar method utilizing B-Mode data if RF data is not available. Analyzing pixel intensity allows abstraction of transducer-specific properties but may require optimizing filter-specific parameters such as the window size [16]. With solely geometric methods, several transducer-specific properties are required [15]. Thus, we combined techniques from both geometric and intensity methods with the transducer pulse width to define a window size as the only required input parameter.

If RF data is available, then the RF data is processed with statistical analysis based on the acoustic physics of shadows. The value in the RF data is that it is the raw signal read by the transducer and is representative of the interactions between the acoustic wave and a shadow boundary. However, many

ultrasound machines do not provide access to the RF data, which is difficult to visualize on a graphic image. Instead, most machines provide only B-Mode data. The machines process the RF data with several nonlinear transformations and filtering to produce an enhanced image for visual interpretation by a clinician. This process obscures many features from the RF signal in favor of visual enhancement, such as by smoothing the grainy patches seen in an RF image. However, these features contain information on how the ultrasound signal interacts with the material and can be leveraged to characterize material properties, such as the presence of tissue. In addition, B-Mode images can be manually enhanced by adjusting parameters such as gain or dynamic range windowing and thus, B-Mode images are subject to operator variability. Thus, we argue that analyzing features such as acoustic shadows from the RF data provides a more consistent and versatile detection.
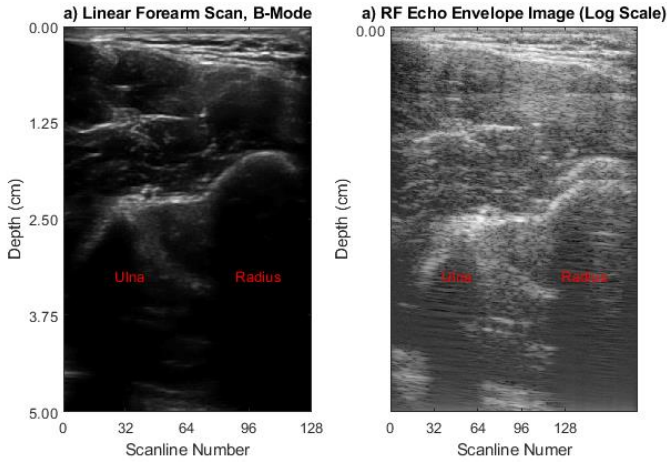

Fig. 2. A comparison of a scan of the forearm from a linear transducer (L14-5/38, Ultrasonix, Canada) with the a) brightness-mode and b) logarithmic echo envelope of the radiofrequency data. The brightness-mode data is visually enhanced to remove the speckle for a smoother image, but the speckle in the radiofrequency data can be leveraged to understand the scattering interactions of the acoustic wave in certain materials.

We also present a scanline statistical analysis on B-Mode data of the same RF data set. This is to provide a shadow detection method in the common scenario where RF data is not available. Similarly with the goal of a minimal-parameter detection method easily usable by different operators. Both detection methods do not require significant configuration between different imaging scenarios, other than adjusting the window of the scanline patch to correspond to the transducer pulse width.

A. Data Collection

Ultrasound B-Mode and RF data was acquired by scanning X adult participants with informed written consent. Each patient was scan on the forearm near the distal end of the pronator quadratus in the supinated position, on the elbow near the cubital fossa in the supinated position, and on the anterior surface of right ribs 11-12 in a laid down position. The scans were taken with a curvilinear (C-5-2/60, Ultrasonix, Canada)

and a linear (L14-5/38, Ultrasonix, Canada) transducer for a total of 6 images per participant. The B-Mode and RF data were then processed by our algorithm to identify regions of acoustic shadowing.

B. Validation

A trained annotator manually outlined regions of acoustic shadow on the B-Mode images. The manually identified shadow regions were used as a gold standard, as manually identifying shadows is common clinical practice and has been used in previous literature for comparison [16]. The pixels of the manually identified shadows were compared with that of the automatically detected shadows to obtain a Dice coefficient to quantify the performance of the detection defined in Eq. 1 and by the confusion matrix in Table 1.

$$D = \frac{2TP}{2TP + FP + FN} \tag{1}$$

TABLE I
DEFINITIONS OF CONFUSION MATRIX

	Shadow Pixel (Manual)	Non-Shadow Pixel (Manual)
Shadow Pixel (Algorithm)	True Positive (TP)	False Positive (FP)
Non-Shadow Pixel (Algorithm)	False Negative (FN)	True Negative (TN)

C. Radiofrequency Speckle Analysis

To detect shadow regions on the RF data, ultrasonic speckle is analyzed to characterize patches of the image. Speckle occurs due to the scattering of acoustic waves in a material, which results in a series of interference from the scattered acoustic waves. B-Mode data commonly attempts to remove speckle from the image for a smoother visualization, but speckle contains information of the acoustic interactions of the material. An acoustic wave scatters differently depending on the material with a different speckle pattern and thus, it is possible to characterize material by analyzing speckle.

There are several models used in previous literature to model the distribution of the speckle. One of the earliest, well known models is modelling speckle as a probability density of the random walk of sinusoidal acoustic waves with a Rayleigh distribution [22].

$$\Phi(x,\sigma) = \frac{x}{\sigma^2} e^{\frac{-x^2}{2\sigma^2}} \tag{2}$$

Where σ is a scaling parameter.

However, the Rayleigh distribution is an ideal model and characterizes fully developed speckle, which does not occur when there is limited scattering [23]. It has been previously shown that the Rayleigh distribution models structures such as blood well but cannot accurately model less homogenous structure such as cardiac tissue [24]. More generalized models such as the Rician distribution [25], Homodyned K-distribution [26], Gamma distribution [27], and Nakagami distribution [28] have also been used to characterize speckle.

Recently, different models have been used to characterize features in ultrasound with success. Byra et al. (2016) classified breast lesions by modelling lesion speckle with the homodyned k-distribution [29] and Ho et al. (2012) modelled liver speckle with the Nakagami distribution to assess liver fibrosis [30].

For detecting acoustic shadows, which have a distinctively different speckle than non-shadow regions, the Nakagami distribution was chosen. The Nakagami distribution provides more generality compared to the Rayleigh, Rician, and Gamma distributions [31] and is computationally efficient compared to the homodyned K-distribution, which requires greater computational complexity for parameter estimation [32]. The Nakagami distribution is modelled by Eq. 3

$$\Phi(x, \mu, \omega) = 2(\frac{\mu}{\omega})^{\mu} \frac{1}{\Gamma(\mu)} x^{(2\mu-1)} e^{\frac{-\mu}{\omega}x^2} \tag{3}$$

Where μ is the shape parameter, $\omega > 0$ is the scale parameter and $\Gamma(\mu)$ is the gamma distribution.
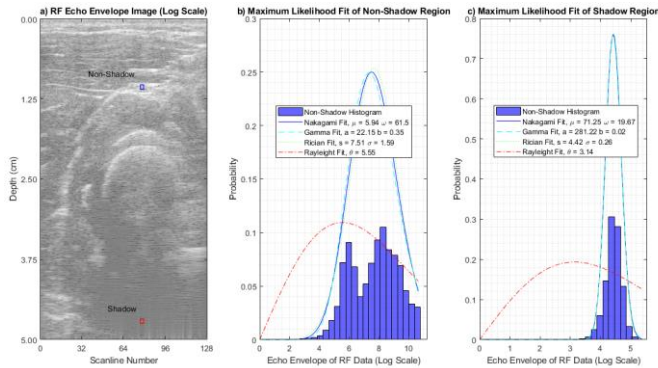

Fig. 3. a) A logarithmic envelope of radiofrequency data of a radial joint taken by a linear (L14-5/38, Ultrasonix, Canada) transducer with a non-shadow and shadow highlighted. Four common statistical distributions are fit onto both the b) non-shadow patch and the c) shadow patch. The Rayleigh distribution is not sufficiently generalized to capture the shape of the distribution curve while the Nakagami, Gamma, and Rician distributions fit much more appropriately. The Nakagami distribution was chosen to characterize the shadows as it proves sufficiently generality while being computationally efficient compared to other distributions.

The RF data for each scan was processed by computing the absolute Hilbert transform of each scanline $f(x)$ and converted to a logarithmic scale.

$$H(t) = \frac{1}{\pi} \int_{-\infty}^{\infty} \frac{f(x)}{t-x} dx \tag{3}$$

The processed RF data then roughly resembles the B-Mode data, but with speckle artefacts present. Each scanline was then segmented into overlapped patches with a width of a single RF data point and a length of three times the pulse width of the transducer. The patch size was chosen from effective patch sizes in previous literature to analyze speckle.
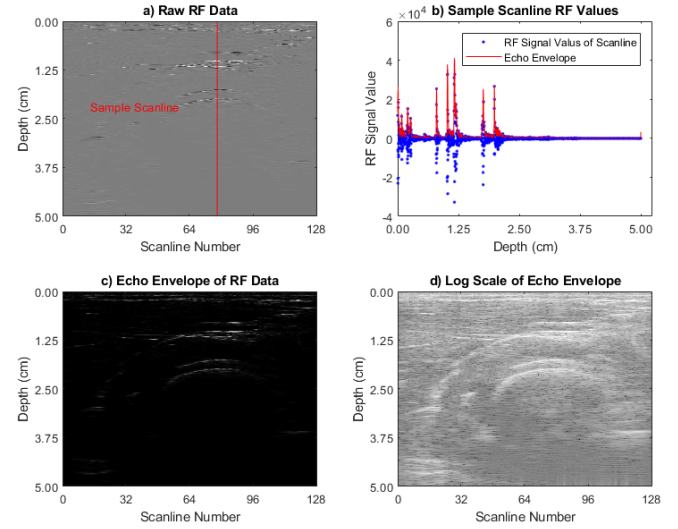

Fig. 4. The processing method for radiofrequency data with a) the raw radiofrequency data with a sample scanline highlighted, b) the echo envelope of the raw radiofrequency data scanline, c) the echo envelope of the entire RF image, and d) the logarithmic scaled echo envelope image. This processing is required for the radiofrequency data to contain statistically distinguishable characteristics between patches to characterize acoustic shadows.

A maximum likelihood estimate (MLE) was computed to fit a Nakagami distribution on each patch to assign each patch with a Nakagami shape and scale parameter to characterize the speckle in each patch.
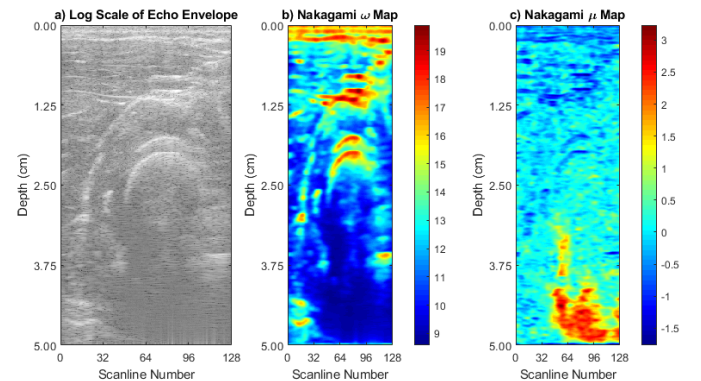

Fig. 5. The corresponding Nakagami parameter map of the RF data of a radial joint image, including a) the logarithmic envelope of the radiofrequency data, b) a map of the Nakagami scale parameter, and c) a map of the Nakagami shape parameter. The Nakagami parameters can be used to characterize regions of the logarithmic RF envelope.

For the purpose of identifying a shadow or non-shadow region, a simple thresholding scheme is sufficient. Non-shadow

regions contain significant speckle whereas shadow regions contain little speckle due to the lack of signal in shadow regions. There still remains slight speckle in shadow regions due to other imaging artefacts that scatter acoustic waves in the shadow region, but the speckle is likely minimal. Thus, shadow detection provides a much simpler problem for speckle analysis as opposed to comparing tissue echotexture for lesions, for instance.

To characterize the shadow and non-shadow regions in the RF image, Otsu's method was applied to compute a threshold for the Nakagami shape and scale parameter for each scanline. Otsu's method provides an automatic thresholding of a data set by computing a threshold value to maximize inter-class variance. This assumes that there exists two statistically significant distributions. In ultrasound images, the intensity distribution of speckle is significantly different than the intensity of minimal speckle in shadow regions. Otsu's method iterates through the range of values for the Nakagami parameters to find the parameter τ in Eq. 4

$$\tau = \{t \mid \sigma_\omega^2(t) = \max(\omega_0(t)\sigma_0^2(t) + \omega_1(t)\sigma_1^2(t))\} \quad (4)$$

$$\omega_0(t) = \sum_{i=0}^{t-1} p(i) \quad (5)$$

$$\omega_1(t) = \sum_{i=0}^{L-1} p(i) \quad (6)$$

Where τ is the computed threshold, t is the iterated values of Nakagami parameters to search for a threshold, and L is the number of bins in the distribution of Nakagami parameters.

The data points of the RF image are then marked as a shadow if there are no further data points axially deeper down the scanline that has a Nakagami parameter above the threshold. This indicates that all data points further than the shadow data point are bright, non-shadow regions. In this way, we avoid mistakenly identifying a temporary dark region that is bright axially deeper, such as a cyst, which is not a shadow as it does not represent a total reflection of the acoustic wave.
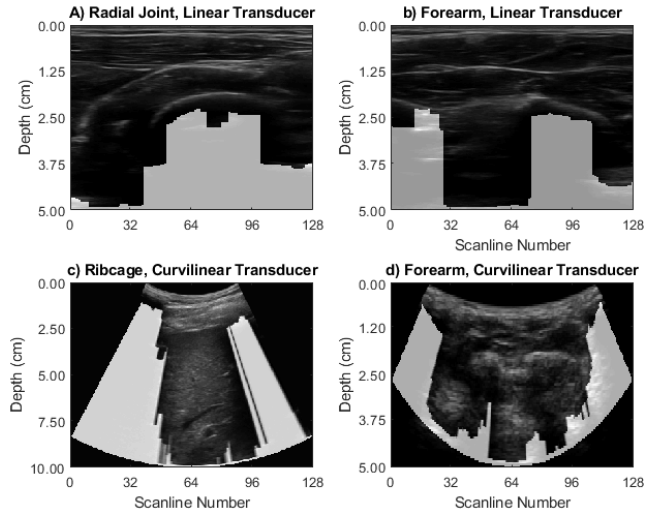

Fig. 6. Examples of RF shadow segmentation with the detected shadows (gray) overlaid on the B-Mode image of different anatomy including the (a) radial joint, and (b) forearm with a linear transducer and the (c) ribcage and (d) forearm with curvilinear transducer. It is important to note that in the b) forearm, linear transducer image that the middle section is not a shadow, but the attenuation of the ultrasound wave in tissue. A shadow is marked by a bright boundary followed by a dark region, which is distinct from a gradually darkening of the image. This is of particular difficulty to identify for novice users and automated shadow detection is of value in these scenarios.

D. B-Mode Scanline Entropy Analysis

Without the RF data, we implement a modified method similar to Hellier et al. (2010) [16] by analyzing the entropy of the image but implement automatic thresholding and remove the need for adaptive filtering. Entropy was chosen as an effective statistical feature as a shadow represents a sudden bright region, due to the almost complete reflection of an acoustic wave, followed by a continuously dark region. This corresponds to a region of high entropy at the boundary, as there is a sudden change in intensity, followed by low entropy, due to the consistent dark pixels.

To detect the acoustic shadows, first, a B-Mode image is segmented to individual scanlines. Then, for each scanline, a local patch for every pixel is created, centered at the pixel. The size of the patch is identical to the size used in the RF method, being three times the pulse width. This size was chosen as an appropriate physical distance to capture sufficient acoustic interaction depending on the pulse width of the transducer. Then, each cumulative entropy of the patch is computed and is assigned to the center pixel.

$$S_{i,j} = \sum_{i=1}^{\eta} I(i-1)\log_2 \frac{I(i-1)}{I(i+1)} + I(i+1)\log_2 \frac{I(i+1)}{I(i-1)} \forall i \in L \quad (7)$$

Where S_i is the symmetric entropy at pixel i on scanline j, L is the set of scanline elements that are not the first or last element, and η is the pulse width of the transducer.

For images from the linear transducer, identifying the path of the scanline is simple as it corresponds to the vertical columns of the image. For the curvilinear transducer, however, the scanlines need to be estimated for the image. It is possible to deduce the geometric transformation from the linear RF data to the curved B-Mode image by creating a map between the data points. However, this is cumbersome and decreases the usability of this method. Instead, a simple linear extrapolation is performed to estimate the direction of the scanline.

For curvilinear images, the algorithm first looks for all the pixels which represent the beginning of a scanline. From the upper left corner, the algorithm then tracks the ultrasonic ring-down, which is a persistent artefact that produces bright bands for a small thickness starting at the top of the image caused by fluid in the transducer that emits a continuous signal to the transducer [33]. With the slope identified on the lateral edge and assuming that the transducer produces a symmetrical image, the algorithm creates scanline paths originating from the first imaging pixel at the top of the image. The slope of the paths are linearly interpolated between the two slopes of the two lateral edges.
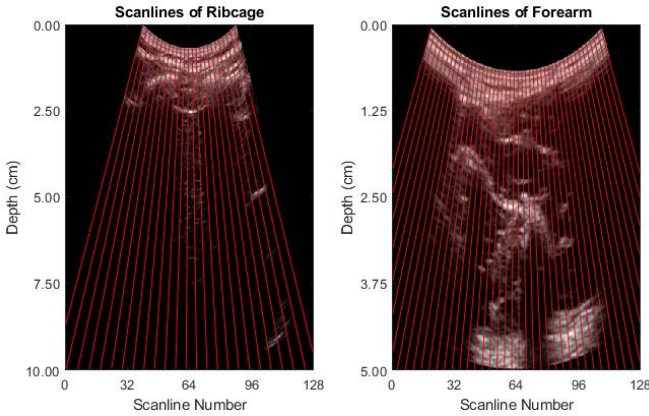

Fig. 7. Creating the scanline paths on a curvilinear ultrasound image of the right ribcage and the forearm with different depth settings on the curvilinear transducers. Two initial paths are creating by computing the slopes of the two lateral edges, which are detected by tracking the ring-down artefact. The remaining paths are creating by linearly interpolating the slope of pixels in between the lateral edges.

Then, Otsu's method is applied similarly to compute an entropy threshold. The significance of the threshold is difference from the RF algorithm. In the RF algorithm, the threshold separates patches of intense speckle and minimal speckle. In the entropy data, however, the threshold separates pixels of a shadow boundary and pixels of non-boundaries, which includes shadow and non-shadow regions.

Then, the last pixel on a scanline with an entropy higher than the threshold is marked as the end of the shadow boundary and all subsequent pixels are marked as a shadow.
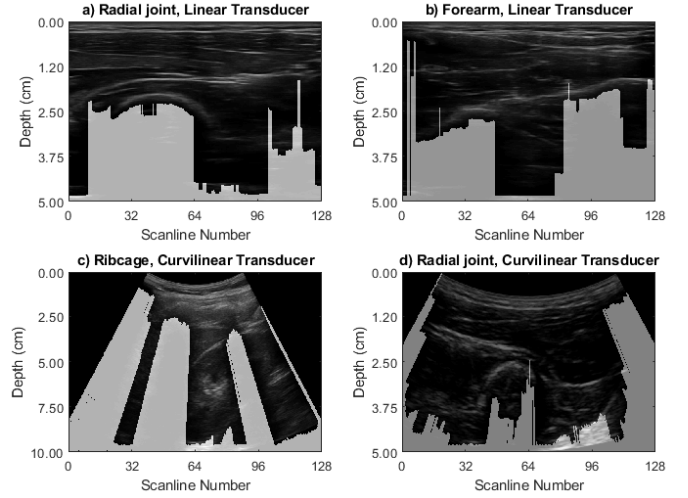

Fig. 8. Examples of B-Mode shadow segmentation with the detection shadows (gray) overlaid on the B-Mode image of different anatomy including the (a) radial joint, and (b) forearm with a linear transducer and the (c) ribcage and (d) forearm with curvilinear transducer.

IV. RESULTS AND DISCUSSION

The dice coefficients for the detected shadows from the RF speckle analysis and the detected shadows from the scanline entropy analysis were 0.93±0.07 and 0.91±0.05 respectively. This is within the upper range of previous methods. However, our method proposed has been applied to different transducer geometries and anatomy, demonstrating versatility of the algorithm. In addition, the proposed method requires only one input parameter from the operator, the pulse width of the transducer, which can be documented for convenient reference. The benefits of such a method would allow for easier use of ultrasound imaging particularly by novice users, who may not have the knowledge of the technical details of several ultrasound parameters required in pure geometric methods of the knowledge of optimizing image processing kernels in pure intensity methods.

The value of analyzing RF data for shadow detection can be demonstrated when applying other methods to ultrasound data with variable operator parameters. For instance, an operator may adjust the time-gain compensation to increase the gain in deeper regions of the image to view tissue in higher intensity. The operator may unintentionally minimize shadowing effects in other areas of the image and any B-Mode analysis method may be unable to identify the artificial bright region as a shadow. As RF data precedes visual image processing, RF data analysis allows consistent quantification of the acoustic signal and is less susceptible to variation from operator adjusted parameters.

There is a notable discrepancy in identifying shadows even with expert annotators in previous literature [15, 16], resulting in the gold standard of manual detection having an upper bound for Dice similarity between annotators. This reflects on the operator variability for the interpretation of ultrasound images and the lack of a robust definition for an acoustic shadow.

Looking closer to an acoustic shadow, the shadow boundary is not a single bright boundary that can clearly defining the start of a shadow. Instead, there is a gradient below and above the shadow boundary, resulting in a pattern of increasingly bright and increasingly dark regions with non-negligible thickness around the boundary.
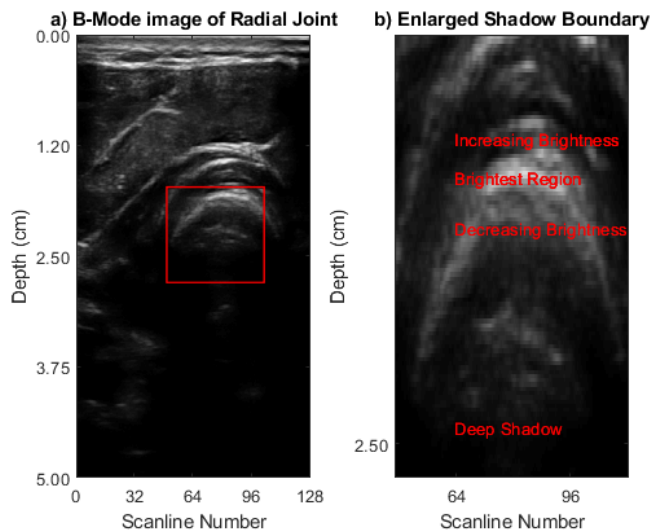

Fig. 9. An annotated image of a radial joint scan with the a) default field of view and b) an enlarged section of the shadow boundary. The shadow boundary is labelled with regions of gradient brightness noted. A shadow boundary is not a single bright line but instead, is a region of increasingly bright to increasingly dark pixels. Hence, it is difficult for even manual annotators to identify exactly where the shadow begins.

There is no consensus as to where the shadow begins. Anatomically, it would be reasonable to define the boundary at the beginning of the gradient to bright region as it may represent the surface of a bone. From a signaling perspective, one may argue that the brightest point in a shadow boundary or where the brightness drops below a certain threshold defines when the signal is significantly reflected. Without a clear definition, there is a limitation in the upper bound of any validation procedure and it would be difficult to compare the performance of algorithms that perform just as well as manual detection. Hence, the focus on this paper was on the versatility and applicability of shadow detection to different scenarios.

V. CONCLUSION

Ultrasound as an imaging modality is becoming further commonplace due to its increased affordability and portability. Ultrasound is difficult to interpret as artefacts such as acoustic shadowing can obscure images. Methods to automatically detect acoustic shadowing from either radiofrequency or brightness-mode data was presented, with a Dice coefficient of 0.93 ± 0.07 and 0.91 ± 0.05 respectively. The method allows identification of shadowing regions, which can be used by inexperienced operators to identify features such as gallstones or bad transducer contact. The method also assists in feature identification for large-scale image processing techniques, such as deep learning training. The performance of the method is comparable to similar shadow detection techniques, with all computations being dynamic except for one adjustable parameter. The versatility of shadow detection to different anatomy and equipment is of particular importance as acoustic shadows occur in many imaging scenarios. Future applications of shadow detection can allow for increased usability of ultrasound where quick detection of anatomical features is required.

REFERENCES

[1] Becker, D. M., Tafoya, C. A., Becker, S. L., Kruger, G. H., Tafoya, M. J., & Becker, T. K. (2016). The use of portable ultrasound devices in low- and middle-income countries: a systematic review of the literature. Tropical Medicine & International Health, 21(3), 294–311.

[2] Bouhemad, B., Brisson, H., Le-Guen, M., Arbelot, C., Lu, Q., & Rouby, J. J. (2011). Bedside ultrasound assessment of positive end-expiratory pressure-induced lung recruitment. American Journal of Respiratory and Critical Care Medicine, 183(3), 341–347.

[3] Tillquist, M., Kutsogiannis, D. J., Wischmeyer, P. E., Kummerlen, C., Leung, R., Stollery, D., Heyland, D. K. (2014). Bedside ultrasound is a practical and reliable measurement tool for assessing quadriceps muscle layer thickness. Journal of Parenteral and Enteral Nutrition, 38(7), 886–890.

[4] Chen, L., Hsiao, A., Langhan, M., Riera, A., & Santucci, K. A. (2010). Use of bedside ultrasound to assess degree of dehydration in children with gastroenteritis. Academic Emergency Medicine, 17(10), 1042–1047.

[5] Iverson, K., Haritos, D., Thomas, R., & Kannikeswaran, N. (2012). The effect of bedside ultrasound on diagnosis and management of soft tissue infections in a pediatric ED. American Journal of Emergency Medicine, 30(8), 1347–1351.

[6] Cubillos, J., Tse, C., Chan, V. W. S., & Perlas, A. (2012). Bedside ultrasound assessment of gastric content: An observational study. Canadian Journal of Anesthesia, 59(4), 416–423.

[7] F. W. Kremkau, K. J. Taylor, "Artifacts in ultrasound imaging", Journal of Ultrasound in Medicine, vol. 5, no. 4, pp. 227-237, 1986.

[8] Sommer, F. G., Filly, R. A., and Minton, M. J, "Acoustic Shadowing Due to Refractive and Reflective Effects", American Journal of Roentgenology, vol. 131, no. 2, pp. 223-226, 1978.

[9] Amin, D. V., Kanade, T., Digioia, A. M., & Jaramaz, B. (2003). Ultrasound registration of the bone surface for surgical navigation. Computer Aided Surgery, 8(1), 1–16.

[10] Good, L. I., Edell, S. L., Soloway, R. D., Trotman, B. W., Mulhern, C., & Arger, P. a. (1979). Ultrasonic properties of gallstones. Effect of stone size and composition. Gastroenterology, 77(2), 258–263. Retrieved from

[11] Drukker, K., Giger, M. L., & Mendelson, E. B. (2003). Computerized analysis of shadowing on breast ultrasound for improved lesion detection. Medical Physics, 30(7), 1833–1842.

[12] [1] B. Dunmire et al., "Use of the Acoustic Shadow Width to Determine Kidney Stone Size with Ultrasound," J. Urol., vol. 195, no. 1, pp. 171–177, 2016.

[12] Ni, D., Chui, Y. P., Qu, Y., Yang, X., Qin, J., Wong, T. T., Heng, P. A. (2009). Reconstruction of volumetric ultrasound panorama based on improved 3D SIFT. Computerized Medical Imaging and Graphics, 33(7), 559–566.

[13] Yan, C. X. B., Goulet, B., Pelletier, J., Chen, S. J. S., Tampieri, D., & Collins, D. L. (2011). Towards accurate, robust and practical ultrasound-CT registration of vertebrae for image-guided spine surgery. International Journal of Computer Assisted Radiology and Surgery, 6(4), 523–537.

[14] Ghose, S., Oliver, A., Mitra, J., Martí, R., Lladó, X., Freixenet, J., Meriaudeau, F. (2013). A supervised learning framework of statistical shape and probability priors for automatic prostate segmentation in ultrasound images. Medical Image Analysis, 17(6), 587–600.

[15] Karamalis, A., Wein, W., Klein, T., & Navab, N. (2012). Ultrasound confidence maps using random walks. Medical Image Analysis, 16(6), 1101–1112.

[16] Hellier, P., Coupé, P., Morandi, X., & Collins, D. L. (2010). An automatic geometrical and statistical method to detect acoustic shadows in intraoperative ultrasound brain images. Medical Image Analysis, 14(2), 195–204.

[17] Drukker, K., Giger, M. L., & Mendelson, E. B. (2003). Computerized analysis of shadowing on breast ultrasound for improved lesion detection. Medical Physics, 30(7), 1833–1842.

[18] Basij, M. (2012). Automatic Shadow Detection in Intra Vascular Ultrasound Images Using Adaptive Thresholding. IEEE International Conference on Systems, Man, and Cybernetics October, 2173–2177.

[19] Santos Filho, E., Saijo, Y., Tanaka, A., & Yoshizawa, M. (2008). Detection and Quantification of Calcifications in Intravascular Ultrasound Images by Automatic Thresholding. Ultrasound in Medicine and Biology, 34(1), 160–165.

[20] Berton, F., Cheriet, F., Miron, M. C., & Laporte, C. (2016). Segmentation of the spinous process and its acoustic shadow in vertebral ultrasound images. Computers in Biology and Medicine, 72, 201–211.

[21] Penney, G. P., Blackall, J. M., Hamady, M. S., Sabharwal, T., Adam, A., & Hawkes, D. J. (2004). Registration of freehand 3D ultrasound and magnetic resonance liver images. Medical Image Analysis, 8(1), 81–91.

[22] F. Milletari et al., "Hough-CNN: Deep learning for segmentation of deep brain regions in MRI and ultrasound," Comput. Vis. Image Underst., vol. 164, pp. 92–102, 2017.

[23] J. Hetherington, V. Lessoway, V. Gunka, P. Abolmaesumi, and R. Rohling, "SLIDE: automatic spine level identification system using a deep convolutional neural network," Int. J. Comput. Assist. Radiol. Surg., vol. 12, no. 7, pp. 1189–1198, 2017.

[22] Burckhardt, C. B. (1978). Speckle in ultrasound B-mode scans. IEEE Transactions on Sonics and Ultrasonics.

[23] Tuthill, T. A., Sperry, R. H., & Parker, K. J. (1988). Deviations from rayleigh statistics in ultrasonic speckle. Ultrasonic Imaging, 10(2), 81–89.

[24] Bernard, O., Touil, B., Gelas, A., Prost, R., and Friboulet, D. (2007). A RBF-Based Multiphase Level Set Method for Segmentation in Echocardiography Using The Statistics of the Radiofrequency Signal. IEEE International Conference on Image Processing.

[25] Crambliu, R. M., & Parker, K. J. (1999). Generation of non-Rayleigh speckle distributions using marked regularity models. IEEE Transactions on Ultrasonics, Ferroelectrics, and Frequency Control, 46(4), 867–874.

[26] Prager, R. W., Gee, A. H., Treece, G. M., & Berman, L. H. (2003). Decompression and speckle detection for ultrasound images using the homodyned k-distribution. Pattern Recognition Letters, 24(4–5), 705–713.

[27] Tao, Z., Tagare, H. D., & Beaty, J. D. (2006). Evaluation of Four Probability Distribution Models for Speckle in Clinical Cardiac Ultrasound Images. IEEE Transactions on Medical Imaging, 25(11), 1483–1491.

[28] Mohana Shankar, P. (2000). A general statistical model for ultrasonic backscattering from tissues. IEEE Transactions on Ultrasonics, Ferroelectrics, and Frequency Control, 47(3), 727–736.

[29] Byra, M., Nowicki, A., Wróblewska-Piotrzkowska, H., & Dobruch-Sobczak, K. (2016). Classification of breast lesions using segmented quantitative ultrasound maps of homodyned K distribution parameters. Medical Physics, 43(10), 5561–5569.

[30] Ho, M. C., Lin, J. J., Shu, Y. C., Chen, C. N., Chang, K. J., Chang, C. C., & Tsui, P. H. (2012). Using ultrasound Nakagami imaging to assess liver fibrosis in rats. Ultrasonics, 52(2), 215–222.

[31] Destrempes, F., & Cloutier, G. (2010). A critical review and uniformized representation of statistical distributions modeling the ultrasound echo envelope. Ultrasound in Medicine and Biology, 36(7), 1037–1051.

[32] Destrempes, F., Porée, J., & Cloutier, G. (2013). Estimation Method of the Homodyned K-Distribution Based on the Mean Intensity and Two Log-Moments. SIAM Journal on Imaging Sciences, 6(3), 1499–1530.

[33] Avruch, L., & Cooperberg, P. L. (1985). The ring-down artifact. Journal of Ultrasound in Medicine : Official Journal of the American Institute of Ultrasound in Medicine, 4(1), 21–28.